

All-optical coherent control of chiral electronic transitions for highly enantioselective photochemistry

Andrés Ordóñez^{1,2,*,†}, Patricia Vindel-Zandbergen³ and David Ayuso^{1,2,4,‡}

¹*Department of Physics, Imperial College London, SW7 2AZ London, UK*

²*Department of Chemistry, Queen Mary University of London, E1 4NS London, UK*

³*Department of Chemistry, New York University, New York 10003, USA*

⁴*Max-Born-Institut, Max-Born-Str. 2A, 12489 Berlin, Germany*

**andres.ordonez@fu-berlin.de*

Enantioselective photochemistry provides access to unique molecular structures and functions, with deep implications for fundamental science and industrial applications. Current methods for highly enantioselective photochemistry critically rely on chiral sensitisers, as circularly polarised light on its own yields vanishingly weak enantioselectivity. Here, we introduce a quantum control strategy to drive highly enantioselective electronic excitations in randomly oriented samples using a pulsed (~ 22 fs) IR laser and two of its harmonics, in the absence of intermediate resonances. Our approach addresses electronic transitions, does not require chiral sensitisers, or cold molecules, or long electronic coherence times, is relevant for liquid-phase samples, and remains effective over interaction regions extending across many laser wavelengths, even in the presence of dispersion. We show how, by 3D shaping the field's polarisation over the interaction region, we can achieve enantioselective coherent control over electronic population transfer. Our ab-initio simulations in the chiral molecule carvone yield a selectivity of $\sim 30\%$ in the populations of the first excited electronic state, three orders-of-magnitude higher than what is possible with circularly polarised light ($\sim 0.01\%$). These results bring all-optical enantioselective photochemistry into the realm of practical applications.

One of the most powerful concepts in physics is the realisation that different systems have different energy spectra. We rely on this not only to distinguish different systems, but also to selectively excite them, with far reaching consequences such as fluorescence microscopy [1–3] and magnetic resonance imaging [4, 5]. However, when two systems differ only by a mirror reflection, like opposite enantiomers (left- and right-handed versions of a chiral molecule), they share the same spectra. Thus, enantioselective excitation requires relying on light's properties beyond the photon energy, such as the photon helicity. This imposes fundamental limitations on our ability to manipulate chiral matter using light, with broad repercussions throughout chemistry and biology.

Beyond their well established role in the pharmaceutical and agrochemical sectors, chiral molecules are emerging as biomarkers for diagnosing diseases including cancer, Alzheimer, and diabetes [6]. Moreover, molecular chirality is rapidly becoming an important asset for nanotechnology [7] in the development of molecular motors [8] and switches [9], spintronic devices [10], and self-assembling structures [11]. However, despite the success and diversity of light-based approaches at distinguishing opposite enantiomers [12–18], achieving highly enantioselective photo-excitation remains very challenging.

For most chiral molecules, the interaction with circularly polarised light leads to excited-state populations differing by less than 0.1% in opposite enantiomers [19, 20]. This difference stems from the interference between electric- and magnetic-dipole interactions [21, 22]. The difference is very small because the magnetic-dipole interaction is usually much weaker than the electric-dipole interaction, and thus their interference is only a small correction to the purely electric-dipole contribution. The so-called superchiral fields aim to amend this problem by considering structured electromagnetic field configurations displaying regions where the ratio of the magnetic- to the electric-field strength is enhanced [23]. However, these regions occur at minima of the electric field intensity and are of deep-sub-wavelength scale, which poses important hurdles for applications [24].

Multiphoton processes offer the opportunity to achieve enantioselective population transfer in the absence of magnetic interactions altogether. Instead of relying on (imbalanced) interference between electric- and magnetic-dipole transitions, a multicolour field can drive an enantiosensitive interference between two (balanced) electric-dipole pathways. This is the essence of the coherent control approach to enantioselective population transfer [25–27], which has been recently implemented (largely independently from previous works) in pioneering experiments using microwaves in the context of rotational transitions in cold (~ 1 K) gas samples [28–31]. By velocity filtering the molecules, a resonant narrow-band (< 1 MHz) UV laser can turn enantioselectivity in rotational states, to enantioselectivity in electronic states, as beautifully shown in Refs. [32, 33]. However, the rotational aspect of this technique and the use

[†] Present address: Department of Physics, Freie Universität Berlin, 14195 Berlin, Germany.

[‡] Present address: Department of Chemistry, Imperial College London, W12 0BZ London, UK.

of narrow-band UV lasers limits it to the gas phase, hindering scaling up the number of excited molecules for practical applications. Furthermore, the narrow-band UV approach is ineffective on molecular species where the excited state is short lived, as is often the case due to radiationless relaxation [34, 35]. Each of these fundamental limitations presents a major hurdle for applications in photochemistry.

Electronic excitation can trigger a broad range of photochemical phenomena such as photoisomerization, photodissociation, and fluorescence. Thus, driving such excitations with high chiral sensitivity naturally leads to all-optical and highly enantioselective photochemistry. This is in stark contrast to current approaches, where the enantioselectivity stems entirely from intricate intermolecular interactions with tailored molecules [36–38]. All-optical approaches would bring distinct advantages with respect to chemical methods in terms of generality, as well as in terms of the temporal and spatial scales on which molecular chirality can be manipulated.

Here we show how to achieve highly enantioselective population transfer between electronic states using current femtosecond laser technology [39, 40], providing a route to enhancing the enantioselectivity of photochemical reactions by three orders of magnitude. Our approach relies on tailoring a light field using only on an intense IR source and two of its harmonics. It requires neither rotationally cold molecules, nor quadruply-resonant excitation, nor narrow band excitation, nor long electronic coherence times, can be extended to liquid samples [41], and is effective throughout interaction regions extending over many wavelengths, even in the presence of dispersion. Thus, we overcome several fundamental limitations of previous proposals [26, 27, 30–33, 42–47] and bring all-optical highly enantioselective photochemistry closer to applications.

Results

We introduce our approach by considering two coherent control schemes that involve a 1- vs 2-photon interference, and a 2- vs 3-photon interference. We consider the enantioselective photoexcitation of an isotropic and racemic sample of chiral molecules. That is, we assume that the molecules are randomly oriented, an equal amount of the two opposite enantiomers, and our objective is to tailor the light to preferentially excite one enantiomer over the other. More precisely, we denote the orientation-averaged populations in the first electronic excited state $|e\rangle$ of the left (S) and right (R) enantiomers as P_e^S and P_e^R , respectively, and we aim to maximise the enantioselectivity as quantified by $\Delta P_e/\bar{P}_e$, where $\Delta P_e \equiv P_e^S - P_e^R$ and $\bar{P}_e \equiv (P_e^S + P_e^R)/2$. First we present the proposed laser setup and the corresponding simulations, and then we explain the analytical model that can be used to rationalise the results.

We illustrate our approach in carvone, a garden-variety chiral molecule that played a central role in the early days of photochemistry [48–53]. Its S form can be found in caraway seeds and its R form in spearmint. Photoexcitation of carvone with visible/UV light triggers its isomerization (see Fig 1a), a common process in organic molecules. The photoisomerization of carvone into carvonecamphor [48, 51–55] was the first example of a [2+2] photocycloaddition, a prominent photochemical reaction [56, 57]. Once excited, both carvone enantiomers are equally likely to isomerise into their respective form of carvonecamphor. Therefore, by making the photoexcitation step enantioselective, i.e. by making $\Delta P_e \neq 0$, one can preferentially trigger one of the two mirror image photochemical reactions (see Fig. 1b).

Figures 1c and d show a 1- vs 2-photon coherent control scheme leading to highly enantioselective excitation. The three frequencies are linearly polarised perpendicular to each other, with the smaller frequency propagating at right angles to the other two, as in the pioneering microwave experiments that demonstrated enantioselective population transfer between rotational states [28, 29]. Unlike in those works, the two-photon pathway does not rely on an intermediate resonance, we use femtosecond pulses, and we focus on electronic excitation in the perturbative regime, where two-pathway coherent control of polyatomic molecules is well established [58]. We use frequencies ω , 2ω , 3ω , with $3\omega = 3.89$ eV resonant with the first electronic excitation. Such phase-locked harmonics can be generated from a single coherent source [40, 59]. By adjusting the relative laser intensities we can balance the weights of the two interfering pathways in Fig. 1c. We keep the pulses relatively short (~ 20 fs) to limit population transfer and stay within the few-photon picture of Fig. 1c, as well as to avoid significant nuclear dynamics, but long enough to avoid few-cycle effects. We find that, since the fields propagate at an angle to each other, their relative phase varies as a function of position across the interaction region. This leads to a spatial oscillation of the interference between the 1- and 2-photon pathways, resulting in sub-wavelength ($\lambda = 2\pi c/\omega = 956$ nm in vacuum) oscillations of $\Delta P_e/\bar{P}_e$ between $\pm 9.2\%$, as captured by our ab-initio simulations (see Methods) shown in the inset of Fig. 1d. That is, the S molecules are preferentially excited in the red regions of Fig. 1d, while the R molecules are preferentially excited in the blue regions, and the centres of blue and red regions are less than a wavelength apart.

The sub-wavelength oscillation of $\Delta P_e/\bar{P}_e$ is a crucial factor when setting up future experiments with optical wavelengths. Indeed, if the measurement spatially averages over red and blue regions, the enantioselectivity will be washed out. Avoiding this requires implementing special procedures, such as confining the interaction region to only red or only blue regions, e.g. by delivering the molecules via a flat liquid micro-jet [60–63] of sub-wavelength thickness and appropriate orientation. As we show in the next subsection, by adjusting the beam geometry, it is possible to

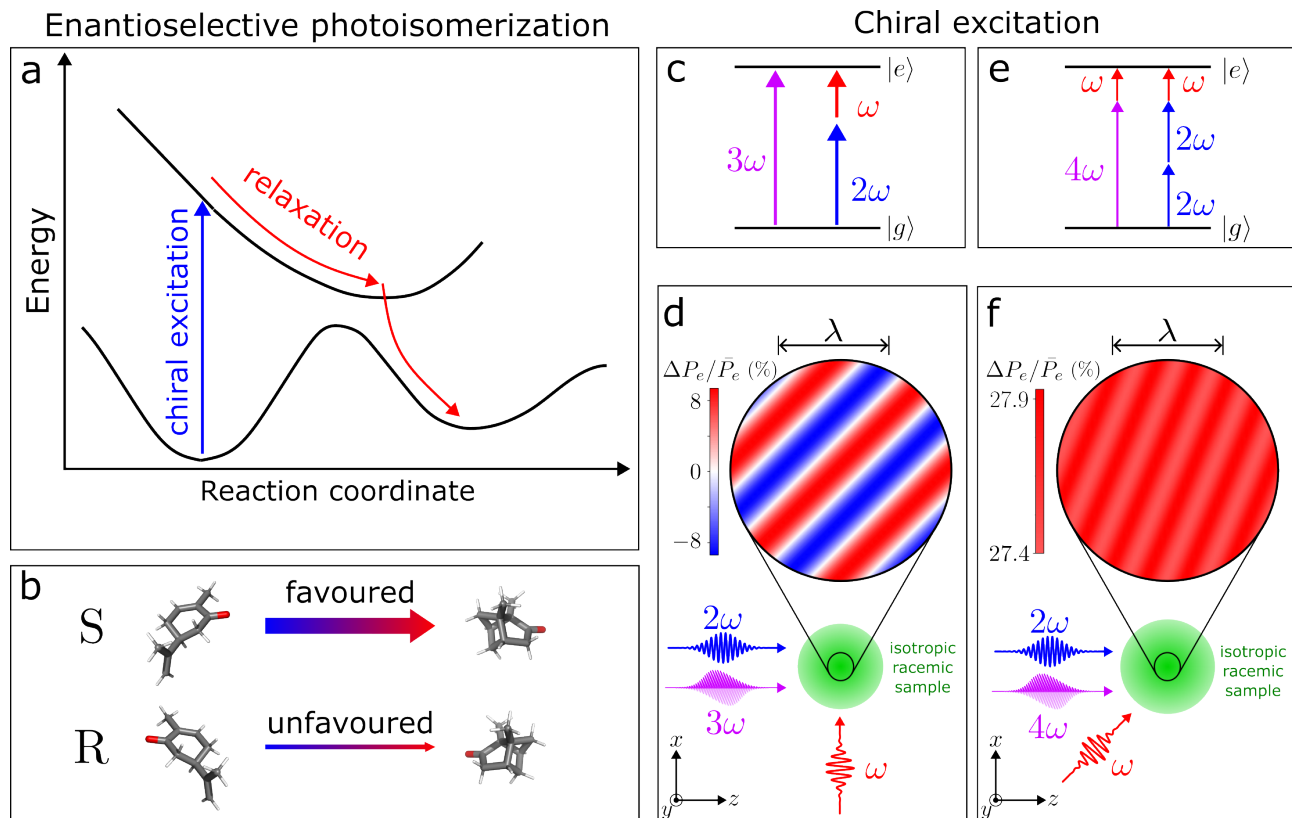


Figure 1. Highly enantioselective photochemistry with nonlinear chiral light-matter interactions. **a.** Scheme for enantioselective photoisomerization with chiral light. Chiral light drives an electronic excitation in a chiral molecule, which then relaxes to a new equilibrium geometry. The potential energy surfaces determining the course of the relaxation process are the same in both enantiomers. Chiral light-matter interaction preferentially excites one of the two enantiomers, thus favouring its photoisomerization. **b.** In carvone, electronic excitation triggers isomerization into carvonecamphor. Enantioselective excitation favours the production of e.g. S carvonecamphor. **c.** Enantioselective excitation of randomly oriented molecules can be achieved in a 1- vs 2-photon coherent-control scheme, provided the field's chirality $h^{(3)}$ [see Eq. (2)] is non zero. **d.** The chiral excitation in **c** can be achieved with linearly polarised laser fields propagating as shown (3ω is polarised along \hat{y}). This approach leads to spatial oscillations of $h^{(3)}$ (occurring on a sub-wavelength scale ($\lambda = 2\pi c/\omega$), which are directly reflected on the enantioselectivity $\Delta P_e/\bar{P}_e = (P_e^S - P_e^R)/[(P_e^S + P_e^R)/2]$ (see inset), where P_e^X is the excited state population of the X enantiomer after the interaction. The inset shows results for Gaussian pulses with full width at half maximum FWHM = 18 fs and peak intensities $I_\omega = I_{2\omega} = 2.1 \times 10^{11}$ W/cm², $I_{3\omega} = 9.4 \times 10^7$ W/cm². **e.** Enantioselective excitation can also be achieved in a 2- vs 3-photon coherent control scheme, provided the field's chirality $h^{(5)}$ [see Eq. (5)] is non zero. **f.** The chiral excitation in **e** can be achieved with linearly polarised laser fields propagating as shown (4ω is polarised along \hat{y}). In the absence of dispersion, this configuration leads to an $h^{(5)}$ which is constant in space, resulting in virtually constant enantioselectivity $\Delta P_e/\bar{P}_e$ across the interaction region (see inset). The inset shows results for Gaussian pulses with FWHM = 22 fs, $I_\omega = 7.3 \times 10^{11}$ W/cm², $I_{2\omega} = 9.4 \times 10^{11}$ W/cm², $I_{4\omega} = 1.6 \times 10^{10}$ W/cm².

significantly increase the spatial period of $\Delta P_e/\bar{P}_e$. However, this comes at the cost of reducing the magnitude of $\Delta P_e/\bar{P}_e$.

We can avoid the sub-wavelength oscillation of $\Delta P_e/\bar{P}_e$ by eliminating the dependence of the two-quantum-pathway interference on the relative phase between frequencies propagating non-collinearly. We achieve this by ensuring that the non-collinear ω contributes one photon to each excitation pathway, as shown in the 2- vs 3-photon scheme in Fig. 1e. This leads to an exact cancellation of the phase of ω in the interference term, which now only depends on the relative phase $\Delta\phi = 2\phi_{2\omega} - \phi_{4\omega}$ between the 2ω and 4ω beams (the control parameter). Interestingly, our analytical and numerical results reveal that for this excitation scheme, having the three polarisations perpendicular to each other yields $\Delta P_e/\bar{P}_e = 0$, in stark contrast to the 1- vs 2-photon scheme. Here we choose the polarisations and propagation directions as depicted in Fig. 1f, with $\omega + 4\omega$ resonant with the first electronic excitation ($\lambda = 2\pi c/\omega = 1.59$ μm). The inset of Fig. 1f shows that $\Delta P_e/\bar{P}_e$ barely oscillates around the value 27.7%. The small oscillation can be attributed to small contributions from other excitation pathways. Changing the relative phase $\Delta\phi$ by π leads to $\Delta P_e/\bar{P}_e = -27.9\%$, i.e. preferential excitation of the opposite enantiomer. The control of $\Delta P_e/\bar{P}_e$ as a function of

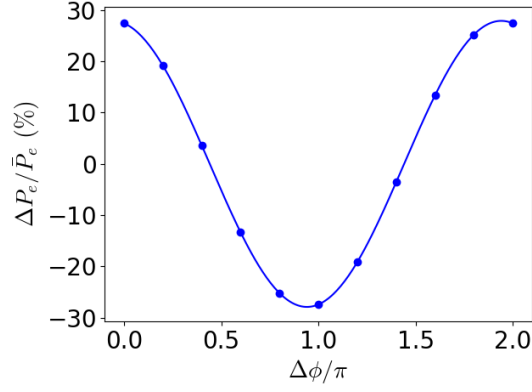


Figure 2. Coherent control of $\Delta P_e/\bar{P}_e$ as a function of the the relative phase $\Delta\phi$ between 2ω and 4ω for the scheme shown in Fig. 1f at a fixed point in space. The dots show calculations and the solid line a fit to $A \cos(\Delta\phi + \delta)$ with $A = 27.9\%$ and $\delta = 0.186$ rad.

$\Delta\phi$ is shown in Fig. 2 at a fixed position in space. For any $\Delta\phi$, the position dependence of $\Delta P_e/\bar{P}_e$ is similar to that shown in Fig. 1f. Thus, our calculations show that by careful design of the excitation scheme, enantioselectivity can be coherently controlled and maintained virtually constant over distances much greater than the wavelength.

Analytical model of enantioselective electronic population transfer

1- vs 2-photon scheme. We write the electric fields as $\vec{E}_j(\vec{r}, t) = \text{Re}\{\vec{E}_j(\vec{r})e^{-i\omega_j t}\}$, $j = 1, 2, 3$, where the complex vector $\vec{E}_j(\vec{r})$ encodes the polarisation, amplitude, and phase associated to frequency ω_j at position \vec{r} . The difference $\Delta P_e \equiv P_e^R - P_e^S$, results from the interference between the two quantum pathways in Fig. 1c and is given by (see Methods)

$$\Delta P_e(\vec{r}) = \text{Re} \left\{ g^{(3)} h^{(3)}(\vec{r}) \right\}, \quad (1)$$

where $g^{(3)}$ is a complex pseudoscalar with opposite signs for opposite enantiomers recording the electronic transition dipoles and detunings, and $h^{(3)}$ is the third-order chiral correlation function characterising the field's chirality relevant for this particular excitation [64],

$$h^{(3)}(\vec{r}) \equiv \vec{E}_3^* \cdot (\vec{E}_1 \times \vec{E}_2), \quad (2)$$

where $\vec{E}_1(\vec{r})$ and $\vec{E}_2(\vec{r})$ drive the two-photon pathway, while $\vec{E}_3(\vec{r})$ drives the one-photon pathway (see Fig. 1c). Equations (1) and (2) show that we can favour the excitation of either S ($\Delta P_e > 0$) or R ($\Delta P_e < 0$) by controlling $h^{(3)}(\vec{r})$. Indeed, $h^{(3)}$ is analogous to the helicity $h = \vec{E}^* \cdot \vec{B}$ emerging in one-photon circular dichroism, with $\vec{E}_1 \times \vec{E}_2$ acting as an effective magnetic field \vec{B} , which is consistent with replacing the magnetic field transition by a two-photon electric-dipole transition.

Equation (2) provides a recipe to maximise $|h^{(3)}|$, and thus ΔP_e , via polarisation shaping. One option is to have the three polarisations linear and perpendicular to each other, as in Fig. 1d. An equally effective choice is to take \vec{E}_2 and \vec{E}_3 circularly polarised and co-rotating, and \vec{E}_1 linearly polarised perpendicular to the plane of circular polarisation (e.g. $\vec{E}_1 \propto \hat{z}$, $\vec{E}_2 \propto \vec{E}_3 \propto \hat{x} + i\hat{y}$). Or \vec{E}_1 and \vec{E}_2 circularly polarised and counter-rotating, and \vec{E}_3 linearly polarised and perpendicular to the plane of circular polarisation (e.g. $\vec{E}_1 \propto \hat{x} + i\hat{y}$, $\vec{E}_2 \propto \hat{x} - i\hat{y}$, $\vec{E}_3 \propto \hat{z}$). All of these choices maximise the triple product in Eq. (2).

For plane-wave fields $\vec{E}_j(\vec{r}) = |E_j|e^{i(\vec{k}_j \cdot \vec{r} - \phi_j)}\hat{e}_j$, we obtain $h^{(3)}(\vec{r}) = \eta^{(3)}e^{i(\Delta\vec{k} \cdot \vec{r} - \Delta\phi)}$, with $\eta^{(3)} \equiv |E_1 E_2 E_3|[\hat{e}_3^* \cdot (\hat{e}_1 \times \hat{e}_2)]$, and $\Delta P_e(\vec{r})$ becomes a plane standing wave,

$$\Delta P_e(\vec{r}) = |g^{(3)}\eta^{(3)}| \cos(\Delta\vec{k} \cdot \vec{r} - \Delta\phi + \delta), \quad (3)$$

where $\Delta\vec{k} \equiv \vec{k}_1 + \vec{k}_2 - \vec{k}_3$, $\Delta\phi \equiv \phi_1 + \phi_2 - \phi_3$, and $\delta \equiv \arg(g^{(3)}\eta^{(3)})$. Thus, $\Delta P_e(\vec{r})$ oscillates in space with a period $\Lambda \equiv 2\pi/|\Delta\vec{k}|$, an amplitude determined by the strength of the chiral light-matter coupling $|g^{(3)}\eta^{(3)}| \propto |\hat{\epsilon}_3^* \cdot (\hat{\epsilon}_1 \times \hat{\epsilon}_2)|$, and a phase controlled by the phase between the two pathways $\Delta\phi$ and the light-matter coupling phase δ . The magnitude $|\hat{\epsilon}_3^* \cdot (\hat{\epsilon}_1 \times \hat{\epsilon}_2)|$ determines the degree of enantioselectivity, while the ‘chiral coherence length’ $\Lambda/2 = \pi/|\Delta\vec{k}|$ determines the distance over which enantioselectivity remains ‘in phase’ and is not washed out by spatial averaging. Thus, it determines the maximum size of the interaction region along $\Delta\vec{k}$ ’s direction.

Equation (3) provides a recipe for maximising the enantioselectivity ΔP_e of the photochemical excitation via light shaping. Ideally, one would like to maximise both the degree of enantioselectivity and the chiral coherence length. Unfortunately, the field polarisation that maximises $|\hat{\epsilon}_3^* \cdot (\hat{\epsilon}_1 \times \hat{\epsilon}_2)|$ minimises Λ , and vice versa. Indeed, achieving a non-zero $|\hat{\epsilon}_3^* \cdot (\hat{\epsilon}_1 \times \hat{\epsilon}_2)|$ with radiation (transverse) fields requires at least one frequency propagating at an angle to the other two, which generally leads to $|\Delta\vec{k}| \neq 0$. For example, in Fig. 1d, the wave vectors $\vec{k}_1 = \omega\hat{x}/c$, $\vec{k}_2 = 2\omega\hat{z}/c$, and $\vec{k}_3 = 3\omega\hat{z}/c$, result in $\Delta\vec{k} = \omega(\hat{x} - \hat{z})/c$, which explains the resulting direction and periodicity ($\Lambda = \lambda/\sqrt{2}$, where $\lambda = 2\pi c/\omega$) of the oscillations of $\Delta P_e/\bar{P}_e$. Finding the right balance between $|\hat{\epsilon}_3^* \cdot (\hat{\epsilon}_1 \times \hat{\epsilon}_2)|$ and Λ requires careful consideration the particular experimental conditions.

Let us illustrate the trade-off between the degree of enantioselectivity and the chiral coherence length by considering the beam arrangement in Fig. 3a, where \vec{k}_1 and \vec{k}_2 are at a variable angle θ and their sum is set parallel to \vec{k}_3 to minimise $|\Delta\vec{k}|$ (maximise Λ). This arrangement provides the maximal Λ for a given $|\hat{\epsilon}_3^* \cdot (\hat{\epsilon}_1 \times \hat{\epsilon}_2)|$. A simple geometrical argument shows that $|\hat{\epsilon}_3^* \cdot (\hat{\epsilon}_1 \times \hat{\epsilon}_2)| = \sin\theta$ and $\Lambda = 2\pi(k_3 - \sqrt{k_1^2 + k_2^2 - 2k_1k_2\cos\theta})^{-1}$. The curves shown in Fig. 3a are for propagation in the absence of dispersion (vacuum, upper curve) and in a typical dispersive medium (liquid water, lower curve), for $\omega_1 = \omega$, $\omega_2 = 2\omega$, $\omega_3 = 3\omega$. Both curves show that an increase in Λ comes with a decrease in $|\hat{\epsilon}_3^* \cdot (\hat{\epsilon}_1 \times \hat{\epsilon}_2)|$. For example, increasing Λ/λ from 1 to 10 comes at the cost of decreasing $|\hat{\epsilon}_3^* \cdot (\hat{\epsilon}_1 \times \hat{\epsilon}_2)|$ from 1 to 0.4 (0.5) in liquid water (vacuum). In liquid water, dispersion brings $|\hat{\epsilon}_3^* \cdot (\hat{\epsilon}_1 \times \hat{\epsilon}_2)|$ to zero at $\Lambda/\lambda = 32$, setting a hard limit on the maximum value of Λ . In the absence of dispersion, the curve flattens out for large values of Λ/λ , and e.g. $|\hat{\epsilon}_3^* \cdot (\hat{\epsilon}_1 \times \hat{\epsilon}_2)| = 0.1$ at $\Lambda/\lambda = 300$. Note that reduction of the maximum enantioselectivity by a factor of 10 may still yield much higher enantioselectivity than circularly polarised light. Therefore, while this scheme is not restricted to sub-wavelength interaction regions, it is most effective for interaction regions smaller than about 5λ in $\Delta\vec{k}$ ’s direction, especially in dispersive media. This scale is within reach of current liquid microjet technology [60–63].

2- vs 3-photon scheme. Applying the same theoretical framework, we obtain (see Methods),

$$\Delta P_e(\vec{r}) = \text{Re} \left\{ \vec{g}^{(5)} \cdot \vec{h}^{(5)}(\vec{r}) \right\}, \quad (4)$$

where, in contrast to Eq. (1), $\vec{g}^{(5)}$ and $\vec{h}^{(5)}$ are vectors (with pseudoscalar components). $\vec{h}^{(5)}$ encodes the field’s handedness relevant for this excitation scheme,

$$\vec{h}^{(5)}(\vec{r}) \equiv \begin{pmatrix} [\vec{E}_2 \cdot (\vec{E}_1 \times \vec{E}_1^*)](\vec{E}_2 \cdot \vec{E}_3^*) \\ [\vec{E}_2 \cdot (\vec{E}_1 \times \vec{E}_3^*)](\vec{E}_2 \cdot \vec{E}_1^*) \\ [\vec{E}_2 \cdot (\vec{E}_1^* \times \vec{E}_3^*)](\vec{E}_2 \cdot \vec{E}_1) \end{pmatrix}, \quad (5)$$

where $\vec{E}_1(\vec{r})$ contributes one photon to each pathway, $\vec{E}_2(\vec{r})$ contributes 2 photons to one pathway, and $\vec{E}_3(\vec{r})$ contributes one photon to the other pathway. In Fig. 1d, \vec{E}_1 , \vec{E}_2 , and \vec{E}_3 correspond to the fields at frequencies $\omega_1 = \omega$, $\omega_2 = 2\omega$, and $\omega_3 = 4\omega$, respectively.

Having a vector of handedness, rather than a single number, reflects that there is more than one independent way to construct a local chirality measure with the five available electric field vectors in the interference term. Each component of $\vec{h}^{(5)}$ is more nuanced than $h^{(3)}$, as they involve not only a triple product but also a dot product. Thus, for a component of $\vec{h}^{(5)}$ to be non-zero, not only three of the electric field vectors must be non-coplanar, the other two must be non-orthogonal. In particular, if the three frequencies are linearly polarised perpendicular to each other, all components of $\vec{h}^{(5)}$ vanish, leading to $\Delta P_e = 0$, in stark contrast to $h^{(3)}$.

A fundamental consequence of the vectorial nature of $\vec{h}^{(5)}$ in Eq. (4) is that the polarisation dependence of ΔP_e is molecule specific. In the case of $h^{(3)}$ and Eq. (1), the dependence of ΔP_e on the polarisations of \vec{E}_1 , \vec{E}_2 , and \vec{E}_3 is the same for all molecules up to a relative phase, it varies as $\vec{E}_3^* \cdot (\vec{E}_1 \times \vec{E}_2)$. However, in the case of $\vec{h}^{(5)}$ and Eq. (4), since each component of $\vec{h}^{(5)}$ is weighted by a different component of $\vec{g}^{(5)}$, and each molecule has a different distribution of $\vec{g}^{(5)}$ components, the behaviour of ΔP_e as a function of the polarisations of \vec{E}_1 , \vec{E}_2 and \vec{E}_3 is molecule specific. The polarisations used in Fig. 1e, $\hat{\epsilon}_1 = (\hat{x} - \hat{z})/\sqrt{2}$, $\hat{\epsilon}_2 = \hat{x}$, $\hat{\epsilon}_3 = \hat{y}$, yield $\vec{h}^{(5)} \propto (0, 1, 1)$. In contrast, choosing ω_1 circularly polarised and ω_2 and ω_3 linearly polarised perpendicular to the plane of circular polarisation yields $\vec{h}^{(5)} \propto (1, 0, 0)$.

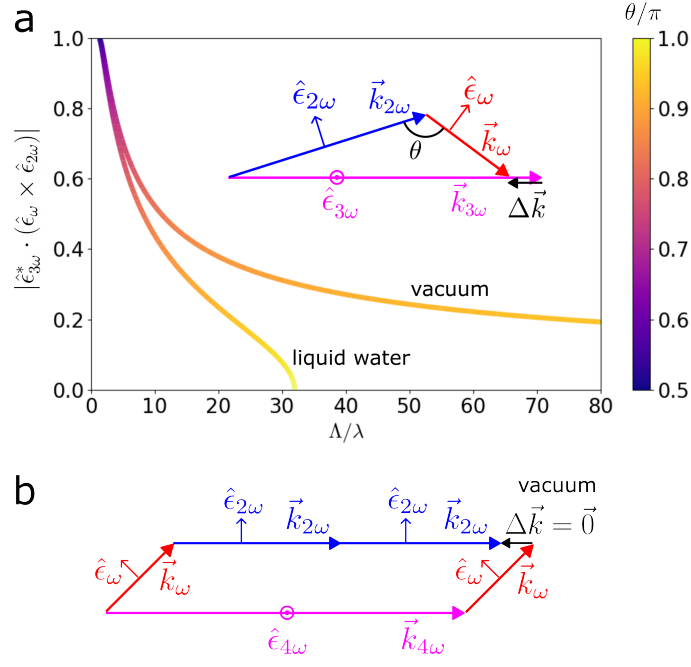


Figure 3. **a.** Trade-off between $|\hat{\epsilon}_{3\omega}^* \cdot (\hat{\epsilon}_\omega \times \hat{\epsilon}_{2\omega})|$ and Λ/λ in a beam arrangement that attempts to maximise both $|\hat{\epsilon}_{3\omega}^* \cdot (\hat{\epsilon}_\omega \times \hat{\epsilon}_{2\omega})|$ and $\Lambda = 2\pi/|\Delta\vec{k}|$, which determine the amplitude and spatial periodicity, respectively, of the enantioselective population ΔP_e in the 1- vs 2-photon control scheme [see Eq. (3)]. The upper curve is in the absence of dispersion and the lower curve assuming the dispersion of liquid water. $\lambda = 2\pi c/\omega = 956$ nm in vacuum and $\lambda = 2\pi c/n\omega = 720$ nm in liquid water. $|\hat{\epsilon}_{3\omega}^* \cdot (\hat{\epsilon}_\omega \times \hat{\epsilon}_{2\omega})| = 1$ when $\Lambda/\lambda = 1.31$ in vacuum and $\Lambda/\lambda = 1.26$ in liquid water. **b.** There is no trade-off in the 2- vs 3-photon control scheme chosen for the simulations in Fig. 1f. This geometry yields $\Lambda/\lambda \rightarrow \infty$ ($|\Delta\vec{k}| = 0$) in the absence of dispersion, and $\Lambda/\lambda = 33$ assuming the dispersion of liquid water, without incurring in reductions of the amplitude of the enantioselective population ΔP_e , determined by $|\hat{\epsilon}_{2\omega} \cdot (\hat{\epsilon}_\omega \times \hat{\epsilon}_{4\omega}^*)|(\hat{\epsilon}_{2\omega} \cdot \hat{\epsilon}_\omega^*)$ [see Eqs. (5) and (6)]. $\lambda = 2\pi c/\omega = 1.59$ μm in vacuum and $\lambda = 2\pi c/n\omega = 1.21$ μm in liquid water.

Such polarisation combination has been recently suggested in Ref. [47]. Alternatively, choosing ω_1 circularly polarised in the arrangement of Fig. 1e yields $\vec{h}^{(5)} \propto (0, -1, 1)$. The merit of each of these polarisation combinations and their corresponding $\vec{h}^{(5)}$ vectors depends on the details of $\vec{g}^{(5)}$, which varies from molecule to molecule and remains to be systematically investigated.

For plane-wave electric fields $\vec{E}_j(\vec{r}) = |E_j|e^{i(\vec{k}_j \cdot \vec{r} - \phi_j)}\hat{\epsilon}_j$, we obtain $\vec{h}^{(5)}(\vec{r}) = \vec{\eta}^{(5)}e^{i(\Delta\vec{k} \cdot \vec{r} - \Delta\phi)}$, where $\vec{\eta}^{(5)}$ is obtained by replacing \vec{E}_j by $|E_j|\hat{\epsilon}_j$ in Eq. (5), and

$$\Delta P_e(\vec{r}) = |\vec{g}^{(5)} \cdot \vec{\eta}^{(5)}| \cos(\Delta\vec{k} \cdot \vec{r} - \Delta\phi + \delta) \quad (6)$$

where $\Delta\vec{k} = 2\vec{k}_2 - \vec{k}_3$, $\Delta\phi = 2\phi_2 - \phi_3$, $\delta = \arg(\vec{g}^{(5)} \cdot \vec{\eta}^{(5)})$. In contrast to the 1- vs 2-photon case, here the ω_1 photon contributes to both pathways. Therefore, ΔP_e does not depend on \vec{k}_1 and we can set $|\Delta\vec{k}| = 0$ by having co-propagating ω_2 and ω_3 (up to dispersion), see Figs. 1f and 3b, without compromising the degree of enantioselectivity, determined by $|\vec{g}^{(5)} \cdot \vec{\eta}^{(5)}|$. Even when including dispersion, we still get $|\Delta\vec{k}| \ll k_2$, leading to chiral coherence lengths $\Lambda/2 \gg \lambda$. For example, in liquid water, for the wavelengths used in Fig. 1f, ΔP_e would oscillate with a spatial period $\Lambda = 2\pi/|\Delta\vec{k}| = 33\lambda$, where $\lambda = 2\pi c/n\omega_1$. Equation (6) also shows that the preferential excitation of S ($\Delta P_e > 0$) or R ($\Delta P_e < 0$) enantiomers can be controlled via the relative phase $\Delta\phi = 2\phi_2 - \phi_3$ of the co-propagating frequencies, in accordance with the numerical results in Fig. 2 showing up to 27.9% enantioselectivity.

Discussion

Coherent control of electronic population in polyatomic molecules has been experimentally demonstrated in gas and liquid samples [58, 65]. Our work brings highly enantioselective population transfer (EPT) in randomly oriented samples with current experimental capabilities [40]. Indeed, state-of-the-art field synthesis [39, 66] can provide optical

pulses carrying multiple frequencies spanning from the UV to the near-IR, with high intensities, and controlled relative phases, at kHz repetition rates [40, 67–71]. Furthermore, the integration of thin liquid sheet technology in femtosecond laser setups [62, 63] allows limiting the interaction region of liquid samples to a few μm , which is the scale over which we have shown that enantioselectivity can be maintained on the order of 10% in 1- vs 2-photon coherent control (Figs. 1d and 3a). This degree of enantioselectivity is three orders of magnitude above that found with circularly polarised light for the same transition [72]. It also outperforms superchiral light, which enhances enantioselectivity by one order of magnitude with respect to circularly polarised light, over regions limited to ~ 10 nm [23, 24]. Our 2- vs 3-photon scheme leads to enantioselectivity close to 30%, maintained throughout tens of μm , and merely requires a stable relative phase between the two co-propagating frequencies. Furthermore, we do not rely on intermediate resonances to achieve these results, which means that (i) unwanted processes resulting from excitation of other states are avoided and (ii) the same setup can be easily adjusted to address a wide range of molecular species.

Our analytical theory reveals the physical mechanism underlying EPT by identifying the relevant molecular and field pseudoscalars, as well as the role of polarisation and propagation for two off-resonant multiphoton excitation schemes. It also provides a simple recipe for controlling and maximising the degree of enantioselectivity via light shaping, according to the specific properties of the molecular sample and the capabilities of each laboratory. The vectorial character of $\vec{h}^{(5)}$ leads to molecule-specific optimisation of the enantioselectivity that goes beyond simply relying on differences in energy-level structure. This offers interesting perspectives for selectively addressing a particular chiral species in mixtures containing molecules with similar spectra. Such mixtures are often unavoidable, as even pure samples of polyatomic species typically exist as a mixture of several conformers with similar energy-level structure.

There are several alternatives to probe EPT to an electronic state. In the case where the excited state decays via isomerization, as in carvone, EPT will favour the creation of one of the two enantiomers of the photoproduct. Thus, starting from a racemic sample, EPT will lead to a non-racemic mixture, both for starting and product molecules [73, 74]. This change can be monitored using standard enantiosensitive methods, either spectroscopically or chemically, as usually done in asymmetric catalysis experiments [38, 75]. Alternatively, if the excited state decays via fluorescence, one could start with an enantiopure sample and monitor how fluorescence changes upon reversal of the field chirality ($h^{(3)}$ or $\vec{h}^{(5)}$), as done with circularly polarised light or superchiral light [23]. Analogously, in the gas phase, instead of measuring fluorescence, one could also probe the excited state population via photoelectron spectroscopy [76], and monitor ionisation yields as a function of $h^{(3)}$ or $\vec{h}^{(5)}$.

Our all-optical femtosecond-laser approach to EPT between electronic states naturally leads to highly enantioselective photochemistry, which offers unique opportunities for chemical synthesis [38]. And since our approach does not rely on chiral sensitizers, it circumvents limitations and challenges intrinsic to intermolecular interactions, such as static enantioselectivity, synthesis of custom chiral sensitizers, and intricate reaction mechanisms. Thus, it offers fundamentally new opportunities, such as rapid switching of enantioselectivity (via phase control). This is a key capability required for the implementation of chiroptical molecular switches [9, 77], which are hindered by the small enantioselectivity obtained with circularly polarised light.

Methods

Simulations

In our simulations, we use the fixed nuclei approximation and the electric-dipole approximation. For a given set of electric field parameters, a fixed molecular orientation, and a fixed point in the interaction region, we expand the electronic wave function in terms of the unperturbed eigenstates and solve the TDSE for the expansion coefficients. The population of the first excited state is then averaged over molecular orientations. We also scan this population as a function of the relative phase between the different frequencies of the electric field. This scan is used to reconstruct the population as a function of molecular position across the interaction region. This reconstruction is exact in the limit of long pulses with planar wave fronts.

We perform electronic structure calculations to compute the transition energies and dipole moments required to solve the TDSE. The structure of the most stable conformer of R carvone was taken from Ref. [72] and reoptimized in the current work for consistency using Density Functional Theory (DFT) [78, 79] with the B3LYP [80, 81] functional and the 6-311G(d,p) [82] basis set available in Gaussian 16 [83]. The excitation energies and transition moments were evaluated for the first 100 excited states using time-dependent DFT with the CAM-B3LYP functional and the d-aug-cc-pVDZ basis set. The transition moments between all excited states were computed with the Multiwfn software [84]. The performance of the CAM-B3LYP functional in the calculation of spectroscopic properties of chiral systems has been discussed in detail in Refs. [85–89] and has been recently shown to predict circular dichroism spectra in

good agreement with results obtained from highly accurate EOM-CCSD calculations [90].

The integration over orientations is carried out using a 14-point Lebedev grid for α and β , and a trapezoidal rule with 9 equally spaced points in γ , for a total of 126 orientations, where α, β, γ are Euler angles in the zyz convention. Increasing the number of orientations to 286 (26-point Lebedev in α and β and 11 in γ) did not lead to any significant change.

For an electric field consisting of several frequencies $\{\omega_j\}_{j=1}^N$, each of them a plane wave propagating along the unit vector \hat{k}_j with speed c_j and phase ϕ_j , we can write

$$\vec{E}(\vec{r}, t; \phi_1, \phi_2, \dots, \phi_N) \equiv \sum_{j=1}^N E_j e^{-i(\omega_j t + \phi_j - \frac{\omega_j}{c_j} \hat{k}_j \cdot \vec{r})} \hat{e}_j. \quad (7)$$

Taking the frequency ω_1 as a reference, one can show that a shift in position $\Delta\vec{r}$ is equivalent to a simultaneous shift of time and of the phases of the rest of frequencies $\Delta\phi_j$, $j = 2, \dots, N$, according to

$$\vec{E}(\vec{r} + \Delta\vec{r}, t; \phi_1, \phi_2, \dots, \phi_N) = \vec{E}(\vec{r}; t + \Delta t; \phi_1, \phi_2 + \Delta\phi_2, \dots, \phi_N + \Delta\phi_N), \quad (8)$$

where

$$\Delta t = -\frac{\hat{k}_1 \cdot \Delta\vec{r}}{c_1}, \quad \Delta\phi_j = \omega_j \left(\frac{1}{c_1} \hat{k}_1 - \frac{1}{c_j} \hat{k}_j \right) \cdot \Delta\vec{r}. \quad (9)$$

An overall time shift of the electric field does not change the final state populations. But the final state populations do depend on the phases ϕ_j . Thus, knowing the populations for all ϕ_j at a given position \vec{r} is enough to recover the populations at any other point $\vec{r} + \Delta\vec{r}$ via Eq. (8). This approximation is valid as long as the temporal envelopes do not change significantly upon the shift by Δt . That is, if the pulse envelopes change on a time scale τ , Eq. (8) is valid provided $|\Delta\vec{r}| \ll c_1 \tau$. Taking c_1 equal to the speed of light in vacuum and $\tau = 100$ fs, this yields $|\Delta\vec{r}| \ll 30 \mu\text{m}$. In our simulations, we use relatively short pulses $\tau \approx 20$ fs for the sake of reducing the computing time and avoiding nuclear dynamics, and thus our reconstruction is strictly valid only for $|\Delta\vec{r}| \ll 6 \mu\text{m}$. However, our approach can be trivially extended to longer pulses and thus bigger $|\Delta\vec{r}|$.

Analytical model for 1- vs 2-photon isotropic chiral coherent control

Consider a chiral molecule interacting with a three-colour field given by $\tilde{E}(t) = \sum_{j=1}^3 \tilde{E}_j(t)$, where $\tilde{E}_j(t) = \mathcal{E}_j(t) \text{Re}\{\vec{E}_j e^{-i\omega_j t}\}$, $\mathcal{E}_j(t)$ describes a smooth temporal envelope and the complex vector \vec{E}_j encodes the amplitude, polarisation, and phase of the frequency ω_j . The frequencies are such that $\omega_1 + \omega_2 = \omega_3$ is resonant with the transition from the ground state $|g\rangle$ to the excited state $|e\rangle$. This leads to three sets of excitation pathways: a one photon pathway $|g\rangle \xrightarrow{\omega_3} |e\rangle$, and two sets of two-photon pathways $|g\rangle \xrightarrow{\omega_2} |n\rangle \xrightarrow{\omega_1} |e\rangle$ and $|g\rangle \xrightarrow{\omega_1} |n\rangle \xrightarrow{\omega_2} |e\rangle$, that differ only by the photon ordering, and where $|n\rangle$ is an intermediate state that has to be summed over. The probability amplitude for state $|e\rangle$ after the interaction is given by

$$a_e = a_e^{(\omega_3)} + \sum_n \left(a_{e,n}^{(\omega_1, \omega_2)} + a_{e,n}^{(\omega_2, \omega_1)} \right), \quad (10)$$

where perturbation theory yields

$$a_e^{(\omega_3)} = A^{(\omega_3)} \left(\vec{d}_{e,g} \cdot \vec{E}_3 \right), \quad (11)$$

$$a_{e,n}^{(\omega_1, \omega_2)} = A_n^{(\omega_1, \omega_2)} \left(\vec{d}_{e,n} \cdot \vec{E}_1 \right) \left(\vec{d}_{n,g} \cdot \vec{E}_2 \right), \quad (12)$$

and $a_{e,n}^{(\omega_2, \omega_1)}$ is given by $a_{e,n}^{(\omega_1, \omega_2)}$ after replacing $A_n^{(\omega_1, \omega_2)}$ by $A_n^{(\omega_2, \omega_1)}$ and exchanging \vec{E}_1 and \vec{E}_2 . Here $\vec{d}_{m,n} \equiv \langle m | \vec{d} | n \rangle$ is the electric dipole transition matrix element, and $A^{(\omega_3)}$, $A_n^{(\omega_1, \omega_2)}$, and $A_n^{(\omega_2, \omega_1)}$ are coupling coefficients that depend

on detunings and on the envelopes of the pulses. The orientation averaged population is given by $P_e \equiv \int d\varrho |a_e|^2$, which contains contributions from all three sets of pathways and their interferences. These can be classified according to the number of photons [i.e. electric-dipole products ($\vec{d} \cdot \vec{E}$)] they contain. If they contain an even number of photons they are not enantiosensitive (i.e. they are the same in opposite enantiomers) whereas if they contain an odd number of photons they are enantiosensitive (i.e. have opposite signs in opposite enantiomers) [91]. The latter result from the interference between the one photon pathway and either of the two-photon pathways. Such interferences contain expressions such as $(\vec{d}_{e,g} \cdot \vec{E}_3)^* (\vec{d}_{e,n} \cdot \vec{E}_1) (\vec{d}_{n,g} \cdot \vec{E}_2)$, involving three photons. The population in R and S enantiomers can thus be written as $P_e^R = \bar{P}_e - \frac{1}{2} \Delta P_e$ and $P_e^S = \bar{P}_e + \frac{1}{2} \Delta P_e$, where $\bar{P}_e = (P_e^R + P_e^S)/2$ is the non-enantiosensitive part and $\Delta P_e/2 = (P_e^S - P_e^R)/2$ is the enantiosensitive part. The latter is given by

$$\frac{1}{2} \Delta P_e = 2\text{Re} \left\{ \int d\varrho a_e^{(\omega_3)*} \sum_n \left(a_{e,n}^{(\omega_1, \omega_2)} + a_{e,n}^{(\omega_2, \omega_1)} \right) \right\} \quad (13)$$

$$= 2\text{Re} \left\{ A^{(\omega_3)*} \sum_n \left(A_n^{(\omega_1, \omega_2)} - A_n^{(\omega_2, \omega_1)} \right) \left[\vec{d}_{e,g}^R \cdot \left(\vec{d}_{e,n}^R \times \vec{d}_{n,g}^R \right) \right] \left[\vec{E}_3^* \cdot \left(\vec{E}_1 \times \vec{E}_2 \right) \right] \right\}, \quad (14)$$

where $\vec{d}_{m,n}^R$ are the dipoles of the R enantiomer. The term $[\vec{d}_{e,g}^R \cdot (\vec{d}_{e,n}^R \times \vec{d}_{n,g}^R)] = -[\vec{d}_{e,g}^S \cdot (\vec{d}_{e,n}^S \times \vec{d}_{n,g}^S)]$ encodes the molecular chirality while $h^{(3)} \equiv [\vec{E}_3^* \cdot (\vec{E}_1 \times \vec{E}_2)]$ encodes the chirality of the field. The triple products in Eq. (14) result from molecular orientation averaging [92]. Equation (14) reduces to Eqs. (1) and (2) by introducing the shorthand notation

$$g^{(3)} \equiv 4A^{(\omega_3)*} \sum_n \left(A_n^{(\omega_1, \omega_2)} - A_n^{(\omega_2, \omega_1)} \right) \left[\vec{d}_{e,g}^R \cdot \left(\vec{d}_{e,n}^R \times \vec{d}_{n,g}^R \right) \right]. \quad (15)$$

The minus sign in $(A_n^{(\omega_1, \omega_2)} - A_n^{(\omega_2, \omega_1)})$ is related to the opposite photon ordering of both contributions and the anti-commutativity of the triple product. In general, $A_n^{(\omega_1, \omega_2)} \neq A_n^{(\omega_2, \omega_1)}$, i.e. the energy structure favours a particular photon ordering. The difference between $A_n^{(\omega_1, \omega_2)}$ and $A_n^{(\omega_2, \omega_1)}$ is very pronounced when the transition to the intermediate state is resonant for one of the two photon orderings. In the other extreme, if the photon energy difference is very small with respect to the detunings, i.e. if $|\omega_1 - \omega_2| \ll |\omega_1 - \omega_{n0}|$, the two photon orderings become indistinguishable, $A_n^{(\omega_1, \omega_2)} \approx A_n^{(\omega_2, \omega_1)}$, $g^{(3)}$ vanishes, and $\Delta P_e = 0$.

For illustrative purposes, we include here the coupling coefficients relevant for identical Gaussian envelopes $\mathcal{E}_m(t) = \exp(-t^2/2\tau^2)$

$$A^{(\omega_3)} = i\sqrt{\frac{\pi}{2}} \tau e^{-\tau^2 \Delta_{eg}^2/2}, \quad (16)$$

$$A_n^{(\omega_1, \omega_2)} = \frac{i\tau^2}{4} e^{-\tau^2 \Delta_{eg}^2/4} \left[2\sqrt{\pi} D_+(\xi) + i\pi e^{-\xi^2} \right], \quad (17)$$

where $\Delta_{eg} \equiv \omega_{eg} - \omega_3$, $\xi \equiv (2\Delta_n - \Delta_{eg})\tau/2$, $\Delta_n \equiv \omega_{n0} - \omega_2$, and $D_+(x) \equiv e^{-x^2} \int_0^x e^{t^2} dt$ is the Dawson function. The expression for $A_n^{(\omega_2, \omega_1)}$ can be obtained from $A_n^{(\omega_1, \omega_2)}$ by exchanging ω_1 and ω_2 .

Analytical model for 2- vs 3-photon isotropic chiral coherent control

In this case, the frequencies are such that $\omega_3 = 2\omega_2$ and $\omega_1 + 2\omega_2$ is resonant with the transition from the ground state $|g\rangle$ to the excited state $|e\rangle$. This leads to six sets of excitation pathways: two 2-photon pathways, $|g\rangle \xrightarrow{\omega_3} |m\rangle \xrightarrow{\omega_1} |e\rangle$ and $|g\rangle \xrightarrow{\omega_1} |m\rangle \xrightarrow{\omega_3} |e\rangle$, and three 3-photon pathways $|g\rangle \xrightarrow{\omega_3} |n\rangle \xrightarrow{\omega_2} |l\rangle \xrightarrow{\omega_1} |e\rangle$, $|g\rangle \xrightarrow{\omega_2} |n\rangle \xrightarrow{\omega_1} |l\rangle \xrightarrow{\omega_3} |e\rangle$, and $|g\rangle \xrightarrow{\omega_1} |n\rangle \xrightarrow{\omega_2} |l\rangle \xrightarrow{\omega_3} |e\rangle$, where $|m\rangle$, $|n\rangle$, and $|l\rangle$ are intermediate states that have to be summed over. The probability amplitude for state $|e\rangle$ after the interaction is given by

$$a_e = \sum_m a_{e,m} + \sum_{nl} a_{e,nl}, \quad (18)$$

where perturbation theory yields

$$a_{e,m} = \sum_{\pi} A_m^{\pi(\omega_1, \omega_3)} \left(\vec{d}_{e,m} \cdot \vec{E}_1^{\pi} \right) \left(\vec{d}_{m,g} \cdot \vec{E}_3^{\pi} \right), \quad (19)$$

$$a_{e,nl} = \sum_{\pi'} A_{nl}^{\pi'(\omega_1, \omega_2, \omega_2)} \left(\vec{d}_{e,n} \cdot \vec{E}_1^{\pi'} \right) \left(\vec{d}_{n,l} \cdot \vec{E}_2^{\pi'} \right) \left(\vec{d}_{l,g} \cdot \vec{E}_2^{\pi'} \right), \quad (20)$$

and the sums are over permutations π and π' of the photon orderings in each pathway. The interference between 2- and a 3-photon pathways will lead to an enantioselective contribution to the orientation-averaged population of the form

$$\frac{1}{2} \Delta P_e = 2 \text{Re} \left\{ \sum_{m,n,l} \sum_{\pi, \pi'} A_m^{\pi(\omega_1, \omega_3)*} A_{nl}^{\pi'(\omega_1, \omega_2, \omega_2)} \int d\varrho \left(\vec{d}_{e,m} \cdot \vec{E}_1^{\pi} \right)^* \left(\vec{d}_{m,g} \cdot \vec{E}_3^{\pi} \right)^* \left(\vec{d}_{e,n} \cdot \vec{E}_1^{\pi'} \right) \left(\vec{d}_{n,l} \cdot \vec{E}_2^{\pi'} \right) \left(\vec{d}_{l,g} \cdot \vec{E}_2^{\pi'} \right) \right\}. \quad (21)$$

The integral over orientations can be performed analytically following Ref. [92] (see e.g. the SI of [91] for a worked out example). Each integral over orientations yields a result of the form $\vec{F} \cdot M \vec{G}$, where \vec{F} (\vec{G}) is a six-dimensional vector of rotational invariants involving triple products and dot products between the electric fields (electric dipole) vectors only, and M is a matrix coupling the molecular and the field invariants. See e.g. Eqs. (24)-(26). The different permutations in Eq. (21) will yield different \vec{F} 's, which complicates interpretation. However, since a permutation of the electric fields \vec{E}_j in the integral over orientations is equivalent to a corresponding permutation of the electric dipoles, we choose to keep the \vec{E}_j 's fixed and permute the dipoles instead. That is, we consider integrals with the form

$$\int d\varrho \left(\vec{d}_{e,m}^{\pi} \cdot \vec{E}_1 \right)^* \left(\vec{d}_{m,g}^{\pi} \cdot \vec{E}_3 \right)^* \left(\vec{d}_{e,n}^{\pi'} \cdot \vec{E}_1 \right) \left(\vec{d}_{n,l}^{\pi'} \cdot \vec{E}_2 \right) \left(\vec{d}_{l,g}^{\pi'} \cdot \vec{E}_2 \right), \quad (22)$$

where the permutations are now among the molecular dipoles. To simplify the expression for \vec{F} , we reorder the dot products in the integral and apply Eq. (24) in Ref. [92] according to

$$\int d\varrho \left(\vec{d}_{n,l}^{\pi'} \cdot \vec{E}_2 \right) \left(\vec{d}_{l,g}^{\pi'} \cdot \vec{E}_2 \right) \left(\vec{d}_{e,n}^{\pi'} \cdot \vec{E}_1 \right) \left(\vec{d}_{e,m}^{\pi} \cdot \vec{E}_1 \right)^* \left(\vec{d}_{m,g}^{\pi} \cdot \vec{E}_3 \right)^* = \vec{F} \cdot M \vec{G}_{\pi, \pi'}, \quad (23)$$

where

$$\vec{F} = \begin{pmatrix} 0 \\ 0 \\ 0 \\ \left[\vec{E}_2 \cdot \left(\vec{E}_1 \times \vec{E}_1^* \right) \right] \left(\vec{E}_2 \cdot \vec{E}_3^* \right) \\ \left[\vec{E}_2 \cdot \left(\vec{E}_1 \times \vec{E}_3^* \right) \right] \left(\vec{E}_2 \cdot \vec{E}_1^* \right) \\ \left[\vec{E}_2 \cdot \left(\vec{E}_1^* \times \vec{E}_3^* \right) \right] \left(\vec{E}_2 \cdot \vec{E}_1 \right) \end{pmatrix}, \quad (24)$$

$$M = \frac{1}{30} \begin{pmatrix} 3 & -1 & -1 & 1 & 1 & 0 \\ -1 & 3 & -1 & -1 & 0 & 1 \\ -1 & -1 & 3 & 0 & -1 & -1 \\ 1 & -1 & 0 & 3 & -1 & 1 \\ 1 & 0 & -1 & -1 & 3 & -1 \\ 0 & 1 & -1 & 1 & -1 & 3 \end{pmatrix}, \quad (25)$$

$$\vec{G}_{\pi,\pi'} = \begin{pmatrix} \left[\begin{matrix} \vec{d}_{n,l}^{\pi'} \cdot \left(\vec{d}_{l,g}^{\pi'} \times \vec{d}_{e,n}^{\pi'} \right) \\ \vec{d}_{n,l}^{\pi'} \cdot \left(\vec{d}_{l,g}^{\pi'} \times \vec{d}_{e,m}^{\pi'} \right) \\ \vec{d}_{n,l}^{\pi'} \cdot \left(\vec{d}_{l,g}^{\pi'} \times \vec{d}_{m,g}^{\pi'} \right) \\ \vec{d}_{n,l}^{\pi'} \cdot \left(\vec{d}_{e,n}^{\pi'} \times \vec{d}_{e,m}^{\pi'} \right) \\ \vec{d}_{n,l}^{\pi'} \cdot \left(\vec{d}_{e,n}^{\pi'} \times \vec{d}_{m,g}^{\pi'} \right) \\ \vec{d}_{n,l}^{\pi'} \cdot \left(\vec{d}_{e,m}^{\pi'} \times \vec{d}_{m,g}^{\pi'} \right) \end{matrix} \right] \begin{pmatrix} \vec{d}_{e,m}^{\pi} \cdot \vec{d}_{m,g}^{\pi} \\ \vec{d}_{e,n}^{\pi} \cdot \vec{d}_{m,g}^{\pi} \\ \vec{d}_{e,n}^{\pi} \cdot \vec{d}_{e,m}^{\pi} \\ \vec{d}_{l,g}^{\pi} \cdot \vec{d}_{m,g}^{\pi} \\ \vec{d}_{l,g}^{\pi} \cdot \vec{d}_{e,m}^{\pi} \\ \vec{d}_{l,g}^{\pi} \cdot \vec{d}_{e,n}^{\pi} \end{pmatrix} \end{pmatrix}. \quad (26)$$

Replacing in the expression for the enantiosensitive contribution to the population, we obtain

$$\frac{1}{2}\Delta P_e = 2\text{Re} \left\{ \vec{F} \cdot M \sum_{m,n,p} \sum_{\pi,\pi'} A_m^{\pi(\omega_1,\omega_3)*} A_{n,l}^{\pi'(\omega_1,\omega_2,\omega_2)} \vec{G}_{\pi,\pi'} \right\}. \quad (27)$$

This equation reduces to Eqs. (4) and (5) if we define

$$\vec{g}^{(5)} \equiv 4M' \sum_{m,n,p} \sum_{\pi,\pi'} A_m^{\pi(\omega_1,\omega_3)*} A_{n,l}^{\pi'(\omega_1,\omega_2,\omega_2)} \vec{G}_{\pi,\pi'}, \quad (28)$$

where $\vec{h}^{(5)}$ is given by the non-zero components of \vec{F} and M' is the matrix consisting of the 4th to 6th rows of M .

ACKNOWLEDGEMENTS

A. O. acknowledges funding from the European Union’s Horizon 2020 research and innovation programme under the Marie Skłodowska-Curie grant agreement No 101029393, and from UK Research and Innovation Engineering and Physical Sciences Research Council EP/Z002834/1. P. V. Z. is grateful to the National Science Foundation for its partial support through the Grants CHE-2054616 and CHE-2054604 and the Simons Foundation for the computational resources. A. O. and D. A. acknowledge funding from the Royal Society URF\R1\201333, URF\ERE\210358 and URF\ERE\231177.

-
- [1] Hell, S. W. Nobel Lecture: Nanoscopy with freely propagating light. *Reviews of Modern Physics* **87**, 1169–1181 (2015).
 [2] Betzig, E. Nobel Lecture: Single molecules, cells, and super-resolution optics. *Reviews of Modern Physics* **87**, 1153–1168 (2015).
 [3] Moerner, W. E. W. E. Nobel Lecture: Single-molecule spectroscopy, imaging, and photocontrol: Foundations for super-resolution microscopy. *Reviews of Modern Physics* **87**, 1183–1212 (2015).
 [4] Lauterbur, P. C. All Science Is Interdisciplinary—From Magnetic Moments to Molecules to Men (Nobel Lecture). *Angewandte Chemie International Edition* **44**, 1004–1011 (2005).
 [5] Mansfield, P. Snapshot Magnetic Resonance Imaging (Nobel Lecture). *Angewandte Chemie International Edition* **43**, 5456–5464 (2004).
 [6] Liu, Y., Wu, Z., Armstrong, D. W., Wolosker, H. & Zheng, Y. Detection and analysis of chiral molecules as disease biomarkers. *Nature Reviews Chemistry* **7**, 355–373 (2023).
 [7] Brandt, J. R., Salerno, F. & Fuchter, M. J. The added value of small-molecule chirality in technological applications. *Nature Reviews Chemistry* **1**, 1–12 (2017).
 [8] Feringa, B. L. The Art of Building Small: From Molecular Switches to Motors (Nobel Lecture). *Angewandte Chemie International Edition* **56**, 11060–11078 (2017).
 [9] Feringa, B. L. *Molecular Switches* (Wiley-VCH Verlag GmbH, 2001).
 [10] Naaman, R., Paltiel, Y. & Waldeck, D. H. Chiral molecules and the electron spin. *Nature Reviews Chemistry* **3**, 250–260 (2019).
 [11] Cho, N. H. *et al.* Bioinspired chiral inorganic nanomaterials. *Nature Reviews Bioengineering* **1**, 88 (2023).
 [12] Ayuso, D., Ordonez, A. F. & Smirnova, O. Ultrafast chirality: The road to efficient chiral measurements. *Physical Chemistry Chemical Physics* **24**, 26962–26991 (2022).
 [13] Rouxel, J. R. & Mukamel, S. Molecular Chirality and Its Monitoring by Ultrafast X-ray Pulses. *Chemical Reviews* (2022).

- [14] Bégin, J.-L. *et al.* Nonlinear helical dichroism in chiral and achiral molecules. *Nature Photonics* **17**, 82–88 (2023).
- [15] Sparling, C. & Townsend, D. Two decades of imaging photoelectron circular dichroism: From first principles to future perspectives. *Physical Chemistry Chemical Physics* (2025).
- [16] Koumarianou, G., Wang, I., Satterthwaite, L. & Patterson, D. Assignment-free chirality detection in unknown samples via microwave three-wave mixing. *Communications Chemistry* **5**, 1–7 (2022).
- [17] Tutunnikov, I. *et al.* Observation of persistent orientation of chiral molecules by a laser field with twisted polarization. *Physical Review A* **101**, 021403 (2020).
- [18] Schwennicke, K. & Yuen-Zhou, J. Enantioselective Topological Frequency Conversion. *The Journal of Physical Chemistry Letters* **13**, 2434–2441 (2022).
- [19] L. Greenfield, J. *et al.* Pathways to increase the dissymmetry in the interaction of chiral light and chiral molecules. *Chemical Science* **12**, 8589–8602 (2021).
- [20] Raucci, U., Weir, H., Bannwarth, C., Sanchez, D. M. & Martínez, T. J. Chiral photochemistry of achiral molecules. *Nature Communications* **13**, 2091 (2022).
- [21] Barron, L. D. *Molecular Light Scattering and Optical Activity* (Cambridge University Press, 2004), 2nd edn.
- [22] Berova, N., Polavarapu, P. L., Nakanishi, K. & Woody, R. W. *Comprehensive Chiroptical Spectroscopy* (Wiley, Hoboken, New Jersey, 2012).
- [23] Tang, Y. & Cohen, A. E. Enhanced Enantioselectivity in Excitation of Chiral Molecules by Superchiral Light. *Science* **332**, 333–336 (2011).
- [24] He, C. *et al.* Dissymmetry enhancement in enantioselective synthesis of helical polydiacetylene by application of superchiral light. *Nature Communications* **9**, 5117 (2018).
- [25] Shapiro, M. & Brumer, P. *Quantum Control of Molecular Processes* (Wiley-VCH, Weinheim, 2012), 2nd edn.
- [26] Gerbasi, D., Brumer, P., Thanopoulos, I., Král, P. & Shapiro, M. Theory of the two step enantiomeric purification of 1,3 dimethylallene. *The Journal of Chemical Physics* **120**, 11557–11563 (2004).
- [27] Leibscher, M. *et al.* Full quantum control of enantiomer-selective state transfer in chiral molecules despite degeneracy. *Communications Physics* **5**, 1–16 (2022).
- [28] Eibenberger, S., Doyle, J. & Patterson, D. Enantiomer-Specific State Transfer of Chiral Molecules. *Physical Review Letters* **118**, 123002 (2017).
- [29] Pérez, C. *et al.* Coherent Enantiomer-Selective Population Enrichment Using Tailored Microwave Fields. *Angewandte Chemie International Edition* **56**, 12512–12517 (2017).
- [30] Pérez, C., Steber, A. L., Krin, A. & Schnell, M. State-Specific Enrichment of Chiral Conformers with Microwave Spectroscopy. *The Journal of Physical Chemistry Letters* **9**, 4539–4543 (2018).
- [31] Sun, W. *et al.* Inducing transient enantiomeric excess in a molecular quantum racemic mixture with microwave fields. *Nature Communications* **14**, 934 (2023).
- [32] Lee, J. *et al.* Quantitative Study of Enantiomer-Specific State Transfer. *Physical Review Letters* **128**, 173001 (2022).
- [33] Lee, J., Abdiha, E., Sartakov, B. G., Meijer, G. & Eibenberger-Arias, S. Near-complete chiral selection in rotational quantum states. *Nature Communications* **15**, 7441 (2024).
- [34] Schuurman, M. S. & Stolow, A. Dynamics at Conical Intersections. *Annual Review of Physical Chemistry* **69**, 427–450 (2018).
- [35] Borne, K. D. *et al.* Ultrafast electronic relaxation pathways of the molecular photoswitch quadricyclane. *Nature Chemistry* **16**, 499–505 (2024).
- [36] Brimiouille, R., Lenhart, D., Maturi, M. M. & Bach, T. Enantioselective Catalysis of Photochemical Reactions. *Angewandte Chemie International Edition* **54**, 3872–3890 (2015).
- [37] Tarafder, A. & Miller, L. Chiral chromatography method screening strategies: Past, present and future. *Journal of Chromatography A* **1638**, 461878 (2021).
- [38] Genzink, M. J., Kidd, J. B., Swords, W. B. & Yoon, T. P. Chiral Photocatalyst Structures in Asymmetric Photochemical Synthesis. *Chemical Reviews* **122**, 1654–1716 (2022).
- [39] Fattahi, H. *et al.* Third-generation femtosecond technology. *Optica* **1**, 45–63 (2014).
- [40] Burger, C. *et al.* Compact and flexible harmonic generator and three-color synthesizer for femtosecond coherent control and time-resolved studies. *Optics Express* **25**, 31130–31139 (2017).
- [41] Brixner, T., Damrauer, N. H., Niklaus, P. & Gerber, G. Photosensitive adaptive femtosecond quantum control in the liquid phase. *Nature* **414**, 57–60 (2001).
- [42] Hoki, K., Kröner, D. & Manz, J. Selective preparation of enantiomers from a racemate by laser pulses: Model simulation for oriented atropisomers with coupled rotations and torsions. *Chemical Physics* **267**, 59–79 (2001).
- [43] Yachmenev, A., Onvlee, J., Zak, E., Owens, A. & Küpper, J. Field-Induced Diastereomers for Chiral Separation. *Physical Review Letters* **123**, 243202 (2019).
- [44] Vitanov, N. V. & Drewsen, M. Highly Efficient Detection and Separation of Chiral Molecules through Shortcuts to Adiabaticity. *Physical Review Letters* **122**, 173202 (2019).
- [45] Torosov, B. T., Drewsen, M. & Vitanov, N. V. Efficient and robust chiral resolution by composite pulses. *Physical Review A* **101**, 063401 (2020).
- [46] Neufeld, O., Hübener, H., Rubio, A. & De Giovannini, U. Strong chiral dichroism and enantiopurification in above-threshold ionization with locally chiral light. *Physical Review Research* **3**, L032006 (2021).
- [47] Ye, C., Sun, Y., Fu, L. & Zhang, X. Phase-matched locally chiral light for global control of chiral light–matter interaction. *Optics Letters* **48**, 5511–5514 (2023).

- [48] Ciamician, G. & Silber, P. Chemische Lichtwirkungen. *Berichte der deutschen chemischen Gesellschaft* **41**, 1928–1935 (1908).
- [49] Schönberg, A. *Preparative Organic Photochemistry* (Springer-Verlag New York Inc., 1968).
- [50] Crimmins, M. T. & Reinhold, T. L. Enone Olefin [2 + 2] Photochemical Cycloadditions. In *Organic Reactions*, chap. 2, 297–588 (John Wiley & Sons, Ltd, 2004).
- [51] Malatesta, V., Willis, C. & Hackett, P. A. Laser-induced cycloadditions: The carvone photoisomerization. *The Journal of Organic Chemistry* **47**, 3117–3121 (1982).
- [52] Tsipi, D., Gegiou, D. & Hadjoudis, E. The intramolecular photocycloaddition carvone \rightarrow carvonecamphor. *Journal of Photochemistry* **37**, 159–166 (1987).
- [53] Zandomeneghi, M., Cavazza, M., Moi, L. & Pietra, F. Laser photochemistry: The intramolecular cyclization of carvone to carvonecamphor. *Tetrahedron Letters* **21**, 213–214 (1980).
- [54] Büchi, G. & Goldman, I. M. Photochemical Reactions. VII. The Intramolecular Cyclization of Carvone to Carvonecamphor. *Journal of the American Chemical Society* **79**, 4741–4748 (1957).
- [55] Brackmann, U. & Schäfer, F. P. Photocyclization of carvone to carvone camphor using rare gas halide lasers. *Chemical Physics Letters* **87**, 579–581 (1982).
- [56] Brimiouille, R. & Bach, T. Enantioselective Lewis Acid Catalysis of Intramolecular Enone [2+2] Photocycloaddition Reactions. *Science* **342**, 840–843 (2013).
- [57] Sarkar, D., Bera, N. & Ghosh, S. [2+2] Photochemical Cycloaddition in Organic Synthesis. *European Journal of Organic Chemistry* **2020**, 1310–1326 (2020).
- [58] Wang, X., Bersohn, R., Takahashi, K., Kawasaki, M. & Kim, H. L. Phase control of absorption in large polyatomic molecules. *The Journal of Chemical Physics* **105**, 2992–2997 (1996).
- [59] Boyd, R. *Nonlinear Optics* (Elsevier, 2008), 3rd edn.
- [60] Galinis, G. *et al.* Micrometer-thickness liquid sheet jets flowing in vacuum. *Review of Scientific Instruments* **88**, 083117 (2017).
- [61] Luu, T. T. *et al.* Extreme-ultraviolet high-harmonic generation in liquids. *Nature Communications* **9**, 3723 (2018).
- [62] Barnard, J. C. T. *et al.* Delivery of stable ultra-thin liquid sheets in vacuum for biochemical spectroscopy. *Frontiers in Molecular Biosciences* **9** (2022).
- [63] Ferchaud, C. *et al.* Interaction of an intense few-cycle infrared laser pulse with an ultrathin transparent liquid sheet. *Optics Express* **30**, 34684–34692 (2022).
- [64] Ayuso, D. *et al.* Synthetic chiral light for efficient control of chiral light–matter interaction. *Nature Photonics* **13**, 866 (2019).
- [65] Brixner, T. & Gerber, G. Quantum Control of Gas-Phase and Liquid-Phase Femtochemistry. *ChemPhysChem* **4**, 418–438 (2003).
- [66] Cirmi, G. *et al.* Optical Waveform Synthesis and Its Applications. *Laser & Photonics Reviews* **17**, 2200588 (2023).
- [67] Mücke, O. D. *et al.* Toward Waveform Nonlinear Optics Using Multimillijoule Sub-Cycle Waveform Synthesizers. *IEEE Journal of Selected Topics in Quantum Electronics* **21**, 1–12 (2015).
- [68] Alismail, A. *et al.* Multi-octave, CEP-stable source for high-energy field synthesis. *Science Advances* **6**, eaax3408 (2020).
- [69] Xue, B. *et al.* A Custom-Tailored Multi-TW Optical Electric Field for Gigawatt Soft-X-Ray Isolated Attosecond Pulses. *Ultrafast Science* **2021** (2021).
- [70] Alqattan, H., Hui, D., Pervak, V. & Hassan, M. T. Attosecond light field synthesis. *APL Photonics* **7**, 041301 (2022).
- [71] Ridente, E. *et al.* Electro-optic characterization of synthesized infrared-visible light fields. *Nature Communications* **13**, 1111 (2022).
- [72] Lambert, J., Compton, R. N. & Crawford, T. D. The optical activity of carvone: A theoretical and experimental investigation. *The Journal of Chemical Physics* **136**, 114512 (2012).
- [73] Balavoine, G., Moradpour, A. & Kagan, H. B. Preparation of chiral compounds with high optical purity by irradiation with circularly polarized light, a model reaction for the prebiotic generation of optical activity. *Journal of the American Chemical Society* **96**, 5152–5158 (1974).
- [74] Meinert, C. *et al.* Photonenergy-Controlled Symmetry Breaking with Circularly Polarized Light. *Angewandte Chemie* **126**, 214–218 (2014).
- [75] Bauer, A., Westkämper, F., Grimme, S. & Bach, T. Catalytic enantioselective reactions driven by photoinduced electron transfer. *Nature* **436**, 1139–1140 (2005).
- [76] Wanie, V. *et al.* Capturing electron-driven chiral dynamics in UV-excited molecules. *Nature* **630**, 109 (2024).
- [77] Huck, N. P. M., Jager, W. F., de Lange, B. & Feringa, B. L. Dynamic Control and Amplification of Molecular Chirality by Circular Polarized Light. *Science* **273**, 1686–1688 (1996).
- [78] Kohn, W., Becke, A. D. & Parr, R. G. Density Functional Theory of Electronic Structure. *The Journal of Physical Chemistry* **100**, 12974–12980 (1996).
- [79] Ziegler, T. Approximate density functional theory as a practical tool in molecular energetics and dynamics. *Chemical Reviews* **91**, 651–667 (1991).
- [80] Lee, C., Yang, W. & Parr, R. G. Development of the Colle-Salvetti correlation-energy formula into a functional of the electron density. *Physical Review B* **37**, 785–789 (1988).
- [81] Becke, A. D. Density-functional exchange-energy approximation with correct asymptotic behavior. *Physical Review A* **38**, 3098–3100 (1988).
- [82] McLean, A. D. & Chandler, G. S. Contracted Gaussian basis sets for molecular calculations. I. Second row atoms, Z=11–18. *The Journal of Chemical Physics* **72**, 5639–5648 (2008).

- [83] Frisch, M. J. *et al.* Gaussian 16 Revision C.01 (2016). Gaussian Inc. Wallingford CT.
- [84] Lu, T. & Chen, F. Multiwfn: A multifunctional wavefunction analyzer. *Journal of Computational Chemistry* **33**, 580–592 (2012).
- [85] Toro, C. *et al.* Two-Photon Absorption Circular Dichroism: A New Twist in Nonlinear Spectroscopy. *Chemistry – A European Journal* **16**, 3504–3509 (2010).
- [86] Toro, C. *et al.* Two-photon absorption circular-linear dichroism on axial enantiomers. *Chirality* **22**, E202–E210 (2010).
- [87] Lin, N., Santoro, F., Zhao, X., Rizzo, A. & Barone, V. Vibronically Resolved Electronic Circular Dichroism Spectra of (R)-(+)-3-Methylcyclopentanone: A Theoretical Study. *The Journal of Physical Chemistry A* **112**, 12401–12411 (2008).
- [88] Lin, N. *et al.* Theory for Vibrationally Resolved Two-Photon Circular Dichroism Spectra. Application to (R)-(+)-3-Methylcyclopentanone. *The Journal of Physical Chemistry A* **113**, 4198–4207 (2009).
- [89] Rizzo, A. & Vahtras, O. Ab initio study of excited state electronic circular dichroism. Two prototype cases: Methyl oxirane and R-(+)-1,1'-bi(2-naphthol). *The Journal of Chemical Physics* **134**, 244109 (2011).
- [90] Andersen, J. H., Nanda, K. D., Krylov, A. I. & Coriani, S. Probing Molecular Chirality of Ground and Electronically Excited States in the UV–vis and X-ray Regimes: An EOM-CCSD Study. *Journal of Chemical Theory and Computation* **18**, 1748–1764 (2022).
- [91] Ordonez, A. F. & Smirnova, O. A geometric approach to decoding molecular structure and dynamics from photoionization of isotropic samples. *Physical Chemistry Chemical Physics* **24**, 13605 (2022).
- [92] Andrews, D. L. & Thirunamachandran, T. On three-dimensional rotational averages. *The Journal of Chemical Physics* **67**, 5026–5033 (1977).